

Multiple-junction quantum cascade photodetectors for thermophotovoltaic energy conversion

Jian Yin and Roberto Paiella*

Department of Electrical and Computer Engineering and Photonics Center, Boston University, 8 Saint Mary's Street, Boston, MA 02215, USA

*rpaiella@bu.edu

Abstract: The use of intersubband transitions in quantum cascade structures for thermophotovoltaic energy conversion is investigated numerically. The intrinsic cascading scheme, spectral agility, and design flexibility of these structures make them ideally suited to the development of high efficiency multiple-junction thermophotovoltaic detectors. A specific implementation of this device concept is designed, based on bound-to-continuum intersubband transitions in large-conduction-band-offset $\text{In}_{0.7}\text{Ga}_{0.3}\text{As}/\text{AlAs}_{0.8}\text{Sb}_{0.2}$ quantum wells. The device electrical characteristics in the presence of thermal radiation from a blackbody source at 1300 K are calculated, from which a maximum extracted power density of 1.4 W/cm^2 is determined. This value compares favorably with the present state-of-the-art in interband thermophotovoltaic energy conversion, indicating that quantum cascade photodetectors may provide a promising approach to improve energy extraction from thermal sources.

©2010 Optical Society of America

OCIS codes: (250.5590) Quantum-well, -wire and -dot devices; (040.5350) Photovoltaic.

References and links

1. R. Paiella, ed., *Intersubband Transitions in Quantum Structures* (McGraw-Hill, New York, 2006).
2. P. F. Baldasaro, J. E. Reynolds, G. W. Charache, D. M. DePoy, C. T. Ballinger, T. Donovan, and J. M. Borrego, "Thermodynamic analysis of thermophotovoltaic efficiency and power density tradeoffs," *J. Appl. Phys.* **89**(6), 3319–3327 (2001).
3. L. M. Fraas, J. E. Avery, H. X. Huang, and R. U. Martinelli, "Thermophotovoltaic system configurations and spectral control," *Semicond. Sci. Technol.* **18**(5), S165–S173 (2003).
4. K. Emery, "Characterizing thermophotovoltaic cells," *Semicond. Sci. Technol.* **18**(5), S228–S231 (2003).
5. B. Wernsman, R. R. Siergiej, S. D. Link, R. G. Mahorter, M. N. Palmisiano, R. J. Wehrer, R. W. Schultz, G. P. Schmuck, R. L. Messham, S. Murray, C. S. Murray, F. Newman, D. Taylor, D. M. DePoy, and T. Rahmlow, "Greater than 20% radiant heat conversion efficiency of a thermophotovoltaic radiator/module system using reflective spectral control," *IEEE Trans. Electron. Dev.* **51**(3), 512–515 (2004).
6. R. R. Siergiej, S. Sinharoy, T. Valko, R. J. Wehrer, B. Wernsman, S. D. Link, R. W. Schultz, and R. L. Messham, "InGaAsP/InGaAs tandem TPV device," *AIP Conf. Proc.* **738**, 480–488 (2004).
7. M. W. Dashiell, J. F. Beausang, H. Ehsani, G. J. Nichols, D. M. DePoy, L. R. Danielson, P. Talamo, K. D. Rahner, E. J. Brown, S. R. Burger, P. M. Fourspring, W. F. Topper, Jr., P. F. Baldasaro, C. A. Wang, R. K. Huang, M. K. Connors, G. W. Turner, Z. A. Shellenbarger, G. Taylor, J. Li, R. Martinelli, D. Donetski, S. Anikeev, G. L. Belenki, and S. Luryi, "Quaternary InGaAsSb thermophotovoltaic diodes," *IEEE Trans. Electron. Dev.* **53**(12), 2879–2891 (2006).
8. L. Bhusal, and A. Freundlich, "GaAsN/InAsN superlattice based multijunction thermophotovoltaic devices," *J. Appl. Phys.* **102**(7), 074907 (2007).
9. M. A. Green, *Third Generation Photovoltaics* (Springer-Verlag, Berlin, 2006).
10. M. Graf, G. Scalari, D. Hofstetter, J. Faist, H. Beere, E. Linfield, D. Ritchie, and G. Davies, "Terahertz range quantum well infrared photodetectors," *Appl. Phys. Lett.* **84**(4), 475–477 (2004).
11. L. Gendron, M. Carras, A. Huynh, V. Ortiz, C. Koeniguer, and V. Berger, "Quantum cascade photodetector," *Appl. Phys. Lett.* **85**(14), 2824–2826 (2004).
12. C. Koeniguer, G. Dubois, A. Gomez, and V. Berger, "Electronic transport in quantum cascade structures at equilibrium," *Phys. Rev. B* **74**(23), 235325 (2006).
13. F. R. Giorgetta, E. Baumann, D. Hofstetter, C. Manz, Q. Yang, K. Köhler, and M. Graf, "InGaAs/AlAsSb quantum cascade detectors operating in the near infrared," *Appl. Phys. Lett.* **91**(11), 111115 (2007).

14. A. Vardi, G. Bahir, F. Guillot, C. Bougerol, E. Monroy, S. E. Schacham, M. Tchernycheva, and F. H. Julien, "Near infrared quantum cascade detector in GaN/AlGaIn/AlN heterostructures," *Appl. Phys. Lett.* **92**(1), 011112 (2008).
15. D. Hofstetter, F. R. Giorgetta, E. Baumann, Q. Yang, C. Manz, and K. Köhler, "Midinfrared quantum cascade detector with a spectrally broad response," *Appl. Phys. Lett.* **93**(22), 221106 (2008).
16. S. Y. Zhang, D. G. Revin, J. W. Cockburn, K. Kennedy, A. B. Krysa, and M. Hopkinson, " λ -3.1 μ m room temperature InGaAs/AlAsSb/InP quantum cascade lasers," *Appl. Phys. Lett.* **94**(3), 031106 (2009).
17. I. Vurgaftman, J. R. Meyer, and L. R. Ram-Mohan, "Band parameters for III-V compound semiconductors and their alloys," *J. Appl. Phys.* **89**(11), 5815–5875 (2001).
18. O. Madelung, ed., *Semiconductors – Basic Data*, second edition (Springer-Verlag, Berlin, 1996).
19. J. Y. Andersson, and L. Lundqvist, "Near-unity quantum efficiency of AlGaAs/GaAs quantum well infrared detectors using a waveguide with a doubly periodic grating coupler," *Appl. Phys. Lett.* **59**(7), 857–859 (1991).
20. R. Köhler, R. C. Iotti, A. Tredicucci, and F. Rossi, "Design and simulation of terahertz quantum cascade lasers," *Appl. Phys. Lett.* **79**(24), 3920–3922 (2001).
21. M. Helm, "The basic physics of intersubband transitions," in *Intersubband Transitions in Quantum Wells: Physics and Device Applications I*, H. C. Liu and F. Capasso, eds. (Academic Press, San Diego, 2000).
22. P. Harrison, *Quantum Wells, Wires and Dots: Theoretical and Computational Physics* (John Wiley & Sons, Chichester, 1999).
23. K. J. Franz, W. O. Charles, A. Shen, A. J. Hoffman, M. C. Tamargo, and C. Gmachl, "ZnCdSe/ZnCdMgSe quantum cascade electroluminescence," *Appl. Phys. Lett.* **92**(12), 121105 (2008).

1. Introduction

Intersubband (ISB) transitions in semiconductor quantum wells (QWs) offer several attractive features for optoelectronic device development [1], particularly in the mid- and far-infrared spectral regions where they can be used to overcome some of the intrinsic limitations of narrow-bandgap materials. In fact, ISB transitions already form the basis of well established devices such as quantum cascade lasers (QCLs) and quantum-well infrared photodetectors (QWIPs). Another device application of mid-infrared light that is currently the subject of strongly revived research interest is thermophotovoltaic (TPV) energy conversion, whereby a photovoltaic detector is used to extract electrical power from heat radiation [2–8]. For a common radiator temperature of about 1000 °C, efficient conversion via interband absorption requires photovoltaic materials with bandgap wavelength of at least 2-3 μ m, and in practice InGaAs(Sb) alloys are typically employed. Here we theoretically show that ISB photovoltaic detectors can also be designed for this application with promising performance characteristics. Specifically, besides providing a convenient way to extend the detection cutoff to longer and longer wavelengths, these devices are ideally suited to the implementation of high-efficiency multiple-“junction” TPV cells.

In general, the maximum energy conversion efficiency of single-junction photovoltaic detectors is ultimately determined by two limiting factors. First, below-bandgap radiation cannot be absorbed and therefore its energy is completely unutilized. Second, while photons of energy well above the bandgap can be efficiently absorbed, only a fraction of their energy is converted into electricity, with the remainder lost to the lattice as the resulting photocarriers relax to the bottom of their respective bands before being collected. Higher limiting efficiencies can therefore be obtained with the use of cascaded multiple junctions of different bandgap energy, each providing efficient conversion of near-bandgap radiation over a different photon-energy range [9]. This approach is already well established, particularly in the context of solar cells, although its implementation is complicated by various material and design issues. Most notably, semiconductors of widely different bandgap energies typically also feature proportionally different lattice constants, so that the number of multiple junctions that can be grown on top of one another is ultimately limited by strain accumulation. Furthermore, the ability to fully exploit the combined potential of cascaded multiple junctions for high efficiency is complicated (and often hindered) by the requirement that their individual photocurrents must be carefully matched to one another.

In this work we study the design and limiting performance of multiple-junction TPV devices based on the quantum cascade photodetector (QCP) concept. QCPs are ISB photovoltaic detectors which have been demonstrated recently with a variety of materials systems [10–15] for applications to thermal and THz imaging. Their basic operating principle is illustrated in the conduction-band diagram of Fig. 1, which corresponds to two repetitions

of a specific QCP structure designed in this work. The processes of photon absorption and photocarrier collection are indicated by the vertical and diagonal arrows, respectively. Under the bias conditions used in this example the photocurrent flows against the voltage drop across the device, which implies that electrical power is correspondingly being delivered to the external circuit.

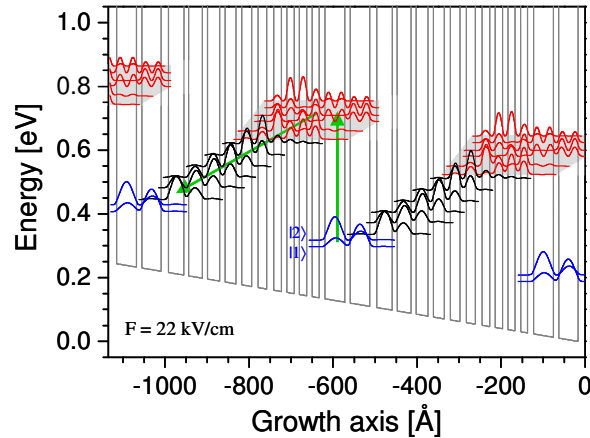


Fig. 1. Γ -valley conduction-band lineup of two adjacent stages based on the QCP2 design of Table 2, and squared envelope functions of the relevant bound states (referenced to their respective energy levels). The electric field $F = 22$ kV/cm across the structure corresponds to the operating point of maximum extracted power (as determined from Fig. 4 below). The processes of photon absorption and photocarrier collection are illustrated by the vertical and diagonal arrows, respectively. The shaded areas indicate the chirped superlattice minibands designed to provide the upper states of the absorptive transitions and to facilitate the initial collection of the photoexcited electrons.

Several properties of QCPs are particularly well suited to the implementation of high-efficiency multiple-junction photovoltaic cells. First, the detection wavelength can be tuned by design over a broad range using the same QW materials system, so that an arbitrarily large number of different stages (“junctions”) can be grown on top of one another with no strain accumulation. Second, each stage provides photodetection over a relatively narrow spectral region, so that the energy of all absorbed photons can be extracted with high efficiency. Finally, the great design flexibility of ISB devices in general allows for accurate control of the current-voltage characteristics of each stage, which in turn simplifies the important problem of current matching. Incidentally, most QCPs demonstrated so far are based on repetitions of identical quantum cascade structures. Recently, a broadband long-wavelength (4.7-7.4 μm) device based on multiple stage architectures has also been reported [15], although the potential of this device concept for thermal energy conversion has not yet been addressed.

The article is organized as follows. In Section 2 we describe a specific implementation of a multiple-junction QCP designed for TPV energy conversion, based on strain-compensated InGaAs/AlAsSb QWs on InP. This device involves four different stage architectures providing photovoltaic detection over four adjacent spectral regions. Each stage is based on a novel QCP design where photocarriers are created via ISB transitions between the two lowest bound states of a coupled-QW structure and the “continuum” of a chirped superlattice miniband (as in the example of Fig. 1). The resulting ability to control the absorption linewidth provides the key design parameter to address the current matching requirement. In Section 3 we present the simulation method used to compute the dark current and photocurrent of each stage as functions of the photovoltage across the stage. The key assumptions and simplifications made in order to derive the device limiting performance are also outlined in this section. The calculated current-voltage characteristics of the individual stages and of the multiple-junction device in the presence of thermal radiation are then presented and discussed in Section 4. From these results, the device ability to produce

electrical power is evaluated and found to compare favorably with the present state-of-the-art in TPV energy conversion. The main conclusions of this study are finally summarized in Section 5.

2. Device design

A key requirement for the development of multiple-junction ISB devices for TPV energy conversion is the use of QWs with sufficiently large conduction-band offset, to allow for ISB absorption of thermal radiation over a sufficiently broad spectral range. Several suitable materials systems exist and have been investigated in recent years for ISB device applications, mainly for the purpose of developing QCLs capable of operation at shorter and shorter wavelengths [1]. In the present work we consider QCP structures based on $\text{In}_{0.7}\text{Ga}_{0.3}\text{As}/\text{AlAs}_{0.8}\text{Sb}_{0.2}$ QWs, which can be grown strain compensated on InP substrates and which have been used recently to demonstrate room-temperature quantum-cascade laser emission down to about 3.1 μm [16]. The material parameters used in the design and modeling of these structures were obtained from Refs. 17 and 18, and are listed in Table 1.

Table 1. Summary of the material parameters used in all simulations presented in this work.

	$\text{In}_{0.7}\text{Ga}_{0.3}\text{As}$	$\text{AlAs}_{0.8}\text{Sb}_{0.2}$
m^*/m_0	0.036	0.148
E_F [eV]	0	1.5
E_X [eV]	0.66	0.76
E_L [eV]	0.62	1.06
ϵ_z	11.8	—
ϵ_0	14.3	—
$\hbar\omega_{LO}$ [meV]	31	—

In $\text{In}_{0.7}\text{Ga}_{0.3}\text{As}/\text{AlAs}_{0.8}\text{Sb}_{0.2}$ multiple QWs grown on InP, the $\text{In}_{0.7}\text{Ga}_{0.3}\text{As}$ well layers have conduction-band minimum in the Γ valley, and the Γ -point conduction-band offset is as large as ~ 1.5 eV [16]. At the same time, however, the $\text{AlAs}_{0.8}\text{Sb}_{0.2}$ barrier layers feature an indirect energy bandgap with conduction-band minima in the X valleys. The effective conduction-band offset ΔE_c of these QWs is therefore determined by the energy difference between the X-valley minima E_X of the barriers and the Γ -valley minimum E_F of the wells, which is estimated to be about 760 meV. Γ -valley confined states with energy above this effective barrier are also supported by the $\text{In}_{0.7}\text{Ga}_{0.3}\text{As}$ wells; however, such states can be expected to be very short lived due to fast leakage into the nearby unbound X-valley states, leading to additional dark current in devices such as the exemplary structure of Fig. 1. Thus, all QCP structures in this work are designed so that their operation only involves Γ -valley bound states with energy below the effective Γ -to-X barrier height ΔE_c . As discussed in the following, this restriction provides the main performance limiting factor of the multiple-junction TPV device modeled in the present study.

The individual stages of this device are based on the “bound-to-continuum” QCP design illustrated in Fig. 1. Specifically, this figure shows the Γ -point conduction-band lineup of two repetitions of the same QCP structure, together with the squared envelope functions of the relevant bound states (referenced to their respective energy levels). A standard Schrödinger-equation solver based on the effective-mass approximation was used to generate these plots. In this structure, the incident radiation is absorbed via ISB transitions from the states labeled |1) and |2) in the figure to the manifold of excited states in the same two QWs. The latter states belong to a chirped superlattice miniband which extends into the four adjacent QWs (as

indicated by the shaded area in the figure), and which provides an efficient path for the initial collection of the photoexcited electrons.

After relaxing to the bottom of the miniband, these electrons are finally transported into the next stage via LO-phonon-assisted transitions through the intervening staircase of bound states. The resulting photocurrent therefore flows from left to right in the figure, producing an open-circuit voltage drop in the opposite direction. To ensure ultrafast transport of the collected photoelectrons, the energy separations between consecutive states in the extractor staircase are nearly resonant to the LO-phonon energy of the QW material (31 meV). Specifically, these energy separations are in the range of 35-41 meV for all QCP structures designed in this study (at their operating point of maximum extracted power). Finally we note that the structure of Fig. 1 also supports bound states in the X and L valleys, which are not shown explicitly to avoid overcrowding the figure; in any case, these states lie at sufficiently high energy above the bottom of the Γ -point QWs (> 620 meV) that they do not provide any additional path for dark current.

Table 2. Layer thicknesses and doping densities of the four QCP structures considered in this work.

	Layer thickness [Å] (Doping density [10^{18} cm $^{-3}$])
QCP1	15 / <u>39</u> (2.1) / 14 / 38 / 18 / 31 / 11 / 28 / 12 / 25 / 13 / 22 / 14 / 20 / 15 / 18 / 16 / 17 / 18 / 14 / 14 / 13 / 14 / 13 / 14 / 13
QCP2	14 / <u>47</u> (1.2) / 13 / 46 / 17 / 37 / 11 / 33 / 12 / 29 / 13 / 26 / 14 / 23 / 15 / 21 / 17 / 18 / 13 / 17 / 13 / 17 / 13 / 17
QCP3	13 / <u>56</u> (0.7) / 13 / 56 / 16 / 43 / 10 / 39 / 11 / 35 / 12 / 31 / 13 / 27 / 16 / 22 / 13 / 21 / 13 / 21 / 13 / 21
QCP4	12 / <u>67</u> (0.5) / 12 / 69 / 15 / 50 / 9 / 44 / 10 / 38 / 11 / 33 / 15 / 27 / 12 / 26 / 12 / 26 / 12 / 26

The specific device modeled in this work is based on four different stage architectures designed for energy conversion from a blackbody radiator at a temperature of 1300 K. Their individual layer thicknesses, starting from the first barrier of the coupled-QW absorption region and moving in the direction of the photocurrent, are listed in units of angstrom in Table 2. Here the bold numbers correspond to the AlAs_{0.8}Sb_{0.2} barriers and the underlined numbers indicate the *n*-type doped layers, with the doping density specified in multiples of 10^{18} cm $^{-3}$ by the subsequent number in parentheses. The structure shown in Fig. 1 is based on the design labeled QCP2 in the table.

These four stage architectures were designed to provide ISB absorption over four adjacent spectral regions within the emission spectrum of the blackbody source. Furthermore, the spectral width of the chirped superlattice miniband was carefully adjusted in each structure so as to control the ISB absorption linewidth and hence the photocurrent. As a result, the stages could be designed so that their output currents at the operating point of maximum extracted power are closely matched to one another. This design flexibility is the main advantage of bound-to-continuum structures in the present context, and is crucial for the purpose of maximizing the combined efficiency of cascaded multiple junctions.

The calculated absorption spectra of the four structures of Table 2 are plotted in Fig. 2 [panels (b) through (e)] together with the emission spectrum of a blackbody source at 1300 K [panel (a)]. The detailed procedure used to compute these traces is described in Section 3 below. Altogether these four structures cover a sizeable fraction of the incident thermal radiation spectrum, extending from about 230 to 540 meV. Additional stages providing ISB absorption at longer wavelengths could in principle be designed; however, these stages would not add appreciably to the total amount of extracted electrical power due to the strong increase in dark current with decreasing transition energy.

On the other hand, the short-wavelength limit of the covered spectral range is limited by the aforementioned requirement that all states involved in the device operation lie at energies below the effective Γ -to- X barrier height ΔE_c . Higher conversion efficiencies could therefore be obtained using QWs with even larger conduction-band offsets, which can be realized for example with III-nitride or II-VI semiconductors. However the ISB device technology of the latter materials systems is still in a relatively early stage, which is why in the present work we consider the more mature family of InGaAs/AlAsSb QWs. Alternatively, the QCP stages of Table 2 could be further integrated with a photovoltaic p - n junction device providing interband absorption at shorter wavelengths. These considerations are discussed in more detail in Section 4 below.

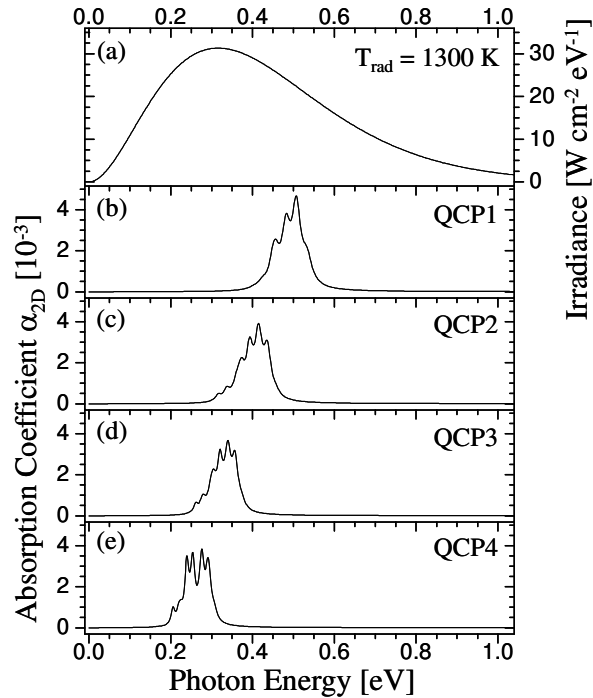


Fig. 2. (a) Emission spectrum of a blackbody source at 1300 K. (b)-(e) Dimensionless absorption spectra of the four QCP structures of Table 2, computed at their respective operating points of maximum extracted power (as determined from Fig. 4 below).

Finally, even though the focus of the present study is on the photovoltaic active material, we briefly consider the issue of how the overall device geometry should be designed to maximize its quantum efficiency. In general, the development of ISB photodetectors is complicated by the well known polarization selection rules of ISB transitions, whereby only TM-polarized radiation is absorbed. A particularly effective way of addressing this issue is to incorporate the absorbing material in a slab waveguide geometry combined with a crossed (doubly periodic) grating coupler. The latter can be fabricated on the device top surface and designed to efficiently scatter the incident radiation into the waveguide guided modes. In fact, QWIP detectors featuring near unity quantum efficiency under normal-incidence illumination with unpolarized light have already been demonstrated with this approach [19]. A similar configuration producing similar results can therefore be envisioned for the device under study. The coupler spectral response can be optimized by controlling the grating depth and duty cycle, and using chirped gratings to further increase its bandwidth if needed. It should also be noted that, unlike ISB photodetectors designed for imaging applications, high-output-power TPV devices generally benefit from relatively large in-plane dimensions (e.g., several

millimeters), which in turn can be expected to facilitate the task of achieving large photon absorption in a grating-coupled planar waveguide geometry.

3. Simulation method

The multiple-junction TPV detector just described is modeled by first computing the photo- and dark-current densities of its individual stages as functions of photovoltage. These quantities are then used to calculate the overall current-voltage characteristics of the multiple-junction device and finally the extracted power versus photovoltage. For the purpose of evaluating the device limiting performance with a relatively simple model, two key assumptions are made in this analysis. First, the photocurrent produced by each stage is computed by assuming that every incident photon with energy within the stage absorption bandwidth is absorbed. It should be noted that this assumption is routinely made in studying the limiting efficiency of photovoltaic energy converters (e.g., see Ref. 9), as it allows isolating the properties of the absorbing material from the detailed device configuration employed. In any case, as discussed in the previous section ISB photodetectors with near-unity polarization-insensitive quantum efficiency are indeed feasible with suitably designed device geometries [19].

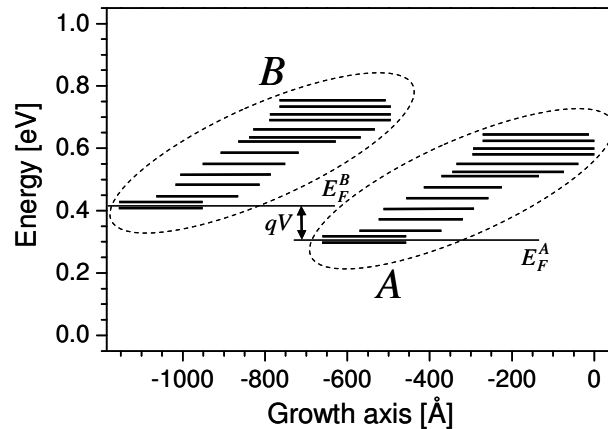


Fig. 3. Schematic illustration of the bound states of two adjacent QCP stages in the presence of photovoltage V . The two sets labeled A and B comprise states that are highly connected to one another by electron/electron and electron/LO-phonon scattering. The quasi-Fermi levels of these two cascades (E_F^A and E_F^B) are also indicated.

To introduce the second key assumption, we refer to the schematic illustration of Fig. 3 where the bound states of two consecutive QCP stages are grouped into two sets (or “cascades”) of highly connected states labeled A and B . Due to the strong coupling among states within each cascade, intra-cascade thermalization is much faster than inter-cascade scattering. As a result, all electrons within each cascade can be assumed to be in a state of quasi-thermal equilibrium with one another, described by a quasi-Fermi level which in the presence of photovoltage is different for the different cascades. In this respect the physics of QCP structures is therefore analogous to that of traditional p - n junctions where the valence and conduction bands similarly support independent thermal distributions [12]. It should be emphasized that this assumption is made even under external illumination when photoelectrons are created in the high-energy states of each cascade. These states have substantial coupling with the low-energy states of the adjacent cascade, so that their inter-cascade scattering rates are in principle not negligible. On the other hand, the presence of a miniband of high-energy states in the design of Fig. 1 implies particularly fast intra-cascade thermalization mediated by electron/electron scattering (which incidentally cannot be readily included in a simple model) in addition to electron/LO-phonon collisions. This is analogous to

the situation of superlattice QCLs, where electron/electron scattering ensures much faster relaxation to the bottom of each lasing miniband than across overlapping minibands [20].

To model the individual QCP structures of Table 2, we begin by evaluating their ISB absorption spectra which can be calculated as follows [21]:

$$\alpha_{2D}(\hbar\omega) = \sum_{i \in A} \sum_{j \in B} \frac{q^2 z_{ij}^2 \omega}{nc\epsilon_0} \frac{\Gamma_{ij}/2}{(E_j - E_i - \hbar\omega)^2 + (\Gamma_{ij}/2)^2} (N_i - N_j). \quad (1)$$

In this equation, α_{2D} is the dimensionless absorption coefficient normalized to the stage inverse thickness $1/t_{st}$; $n = \sqrt{\epsilon_\infty}$ is the refractive index; the two summation indexes i and j run over all states of two consecutive cascades A and B , respectively; the energy at the bottom of subband i (E_i) is computed by solving the Schrödinger equation for the given QCP structure; the dipole moment matrix element between subbands i and j (qz_{ij}) is calculated from their respective envelope functions; the absorption full width at half maximum of the i -to- j transition (Γ_{ij}) is taken to be a fixed fraction (5%) of the transition energy $E_j - E_i$, in accordance with typical measurements from similar QWs [21]; finally, the electron sheet density of subband i (N_i) and the corresponding quasi-Fermi energy E_F^A are obtained by assigning N_D electrons to all subbands of cascade A according to a quasi-Fermi distribution (N_D being the donor sheet density per stage). Throughout this work, the device temperature T is taken to be 300 K.

With this procedure we obtain the spectra plotted in Fig. 2, where peak absorption coefficients α_{2D} of $3\text{--}5 \times 10^{-3}$ per stage are observed. If these QCP structures are embedded in a planar waveguide with a typical guided-mode thickness t_{wg} of about 1 μm and lateral dimensions L of several millimeters, the corresponding modal absorbance $(\alpha_{2D}/t_{st})(t_{st}/t_{wg})L$ has peak values of about 10 or larger per stage. In this case, a single repetition of each QCP structure within the waveguide core is therefore sufficient to provide nearly complete absorption of the in-coupled light over the structure absorption bandwidth. The simulations presented in this article refer to such a situation. Alternatively, one could use N repetitions of each QCP structure grown on top of one another, resulting in an N -fold decrease in photocurrent compensated by a proportional increase in cumulative photovoltage.

The photocurrent density produced by each stage is then calculated as follows:

$$J_p = q \int_{BW} d\varepsilon \frac{2\pi}{h^3 c^2} \frac{\varepsilon^2}{\exp(\varepsilon/k_B T_{rad}) - 1}, \quad (2)$$

where the quantity inside the integral is the well known expression for the photon flux per unit energy emitted by a blackbody radiator of temperature T_{rad} (1300 K in the present case). The integration range is the absorption bandwidth (BW) of the given stage, which here is defined as the spectral region over which the stage absorption coefficient α_{2D} [as determined from Eq. (1)] is larger than 2×10^{-3} . While the specific choice of this threshold value is somewhat arbitrary, we notice that it is large enough to justify the assumption of complete absorption with a single stage. Furthermore, the relatively steep edges of the calculated absorption spectra make the integration limits of Eq. (2) rather insensitive to the specific choice of threshold. The calculated photocurrent densities are found to exhibit a weak but finite dependence on the voltage across the stage, which is due to the changes in subband energies and envelope functions, and therefore in absorption spectra, with varying voltage. We also note that by design there is no overlap among the absorption bandwidths BW of the four structures of Table 2.

Finally, the dark current density produced by each stage is computed using the model developed in Ref. 12, based on the net transfer of electrons between two consecutive cascades A and B via LO-phonon scattering. While all possible pairings of initial and final subbands are included in the simulations, only a few give an appreciable contribution based on the interplay

between their mutual envelope-function overlap and the occupation probability of the initial state. The resulting dark current density J_d can be written as a function of voltage V in the form of a diode equation

$$J_d = J_0 \left(e^{qV/k_B T} - 1 \right), \quad (3)$$

where the reverse saturation current density J_0 is given by

$$J_0 = \sum_{i \in A} \sum_{j \in B} \frac{qm^*}{\pi \hbar^2} \int_{E_i}^{\infty} d\varepsilon \left\{ R_{ij}^{abs}(\varepsilon) n_0 f_i(\varepsilon) [1 - f_j(\varepsilon + \hbar\omega_{LO})] + R_{ij}^{emiss}(\varepsilon) (n_0 + 1) f_i(\varepsilon) [1 - f_j(\varepsilon - \hbar\omega_{LO})] \right\}. \quad (4)$$

Referring to Fig. 1, the quantities J_d and V introduced in these equations are defined to be positive when electrons flow from left to right and when the conduction-band edge increases from right to left, respectively. The exponential increase in dark current with increasing voltage in Eq. (3) is due to the resulting redistribution of the electrons within each cascade into states of higher and higher energy, which have a larger and larger overlap with the states of the adjacent cascade downstream. In Eq. (4), m^* and $\hbar\omega_{LO}$ are the electronic effective mass and the LO-phonon energy of the QW material; $n_0 = 1 / (e^{\hbar\omega_{LO}/k_B T} - 1)$ is the equilibrium number of LO phonons at the detector temperature T of 300 K; $f_i(\varepsilon) = 1 / (e^{(\varepsilon - E_F^i)/k_B T} + 1)$ is the quasi-Fermi distribution function of subband i in cascade A; $R_{ij}^{abs}(\varepsilon)$ and $R_{ij}^{emiss}(\varepsilon)$ are the probabilities per unit time per unit volume that an electron makes a transition from an initially occupied state of energy ε in subband i to an initially empty state in subband j via LO-phonon absorption and emission, respectively. The latter quantities depend on the subband energies and envelope functions, and are computed following Ref. 22.

4. Results and discussion

The procedure just described was used to compute the total current density $J_{tot} \equiv J_p - J_d$ as a function of photovoltage V for each QCP structure of Table 2. The resulting electrical characteristics are shown in Fig. 4(a). For simplicity, each trace here was computed by considering two adjacent cascades based on the same design, as in the example of Fig. 1. If only one repetition of each structure is used in the multiple-junction device, the staircase of bound states funneling electrons from each stage to the next should be properly modified. In any case, these states play a negligible role in the calculated dark and photo-current densities so that their detailed energies and envelope functions are not important. We also note that the observed fluctuations in J_{tot} with V (superimposed to the expected diode-like exponential behavior) are due to the voltage dependence of the QW subband structure, and hence of α_{2D} , R_{ij}^{abs} , and R_{ij}^{emiss} .

If each stage were to be used by itself, the electrical power density correspondingly extracted from the incident thermal radiation would be determined by the stage electrical characteristics as the product $J_{tot}V$. The resulting plots of output power density versus photovoltage are shown in Fig. 4(b). The operating points where these extracted powers are maxima are indicated by the symbols in Fig. 4, and can be seen to occur at roughly the same current density of about 4.2 A/cm² for all four stage architectures. As already mentioned, this is the result of carefully tailoring the ISB absorption spectra of Fig. 2, and ensures optimal performance of the combined TPV device comprising the series combination of the four QCP structures. Specifically, in this case the maximum output power of the combined device is as large as the sum of the maximum output powers of its individual stages, which adds up to about 1.4 W/cm².

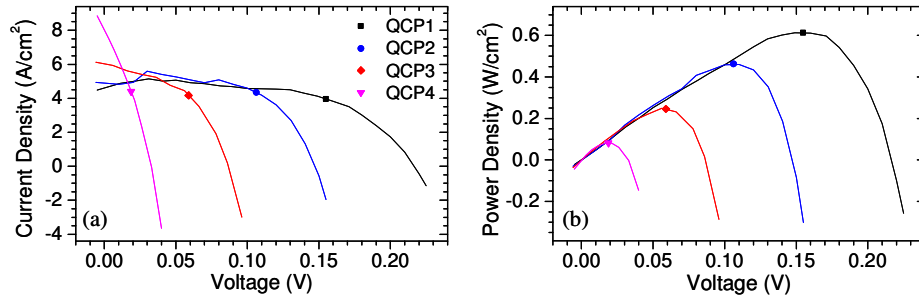


Fig. 4. (a) Total current density $J_{tot} \equiv J_p - J_d$ versus photovoltage V for each QCP structure of Table 2, in the presence of thermal radiation from a blackbody source at 1300 K. The symbol on each trace indicates the operating point where the electrical power density $J_{tot}V$ produced by the corresponding structure is maximum. (b) Output power density $J_{tot}V$ versus photovoltage for the same QCP structures of (a).

The electrical characteristics of the multiple-junction device are shown by the dashed line in Fig. 5. This trace was obtained by adding the photovoltages of the four QCP structures for each value of J_{tot} , starting from exponential fits to the data of Fig. 4(a). Incidentally it should be noted that in general the electric fields present in the four cascaded structures at any operating point of the combined device are different due to their different electrical characteristics. The solid line in Fig. 5 is the corresponding extracted power density $P = J_{tot}V_{tot}$ plotted versus the combined photovoltage V_{tot} . The short-circuit current density, open-circuit voltage, and fill factor obtained from this figure are 4.9 A/cm², 0.48 V, and 59%, respectively; the maximum extracted power density is 1.4 W/cm² as expected.

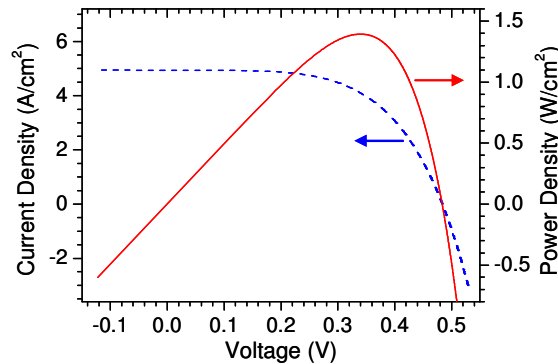


Fig. 5. Total current density $J_{tot} \equiv J_p - J_d$ versus combined photovoltage V_{tot} for the multiple-junction device comprising the four QCP structures of Table 2 connected in series (dashed line), and corresponding output power density $P = J_{tot}V_{tot}$ versus photovoltage V_{tot} (solid line).

By comparison, the present state-of-the-art in TPV energy conversion from a thermal source at the same temperature of 1300 K is about 0.8 W/cm², obtained with a 0.6-eV-bandgap-energy InGaAs interband photodetector grown lattice mismatched on InP with an InPAs buffer [5]. We can therefore conclude that the multiple-junction ISB device concept considered in this work has the potential to provide a substantial improvement over existing technologies. Incidentally, here we use extracted power density rather than conversion efficiency as the main figure of merit, since in the case of TPV systems conversion efficiency depends on several factors other than the photodetector properties, including the use of filters to recuperate the non-absorbable radiation [3].

For a comparison with the limiting performance of interband devices, a suitable reference is a double-junction InGaAs TPV detector with one stage lattice matched to the InP substrate (whereas tandem cells with two or more lattice mismatched junctions do not appear to be practical at present due to structural quality issues [6]). Such a device has been numerically

studied in Ref. 8, where a maximum extracted power of about 1 W/cm^2 from a thermal radiator at 1350 K was computed. The results presented in Figs. 4 and 5 correspond to a lower blackbody-source temperature of 1300 K; by repeating these calculations for the same multiple-junction QCP device in the presence of 1350-K thermal radiation we obtain a maximum output power of over 1.6 W/cm^2 , which again represents a substantial improvement.

Regarding the prospects for further gains, first it should be noted that the $\text{In}_{0.7}\text{Ga}_{0.3}\text{As}/\text{AlAs}_{0.8}\text{Sb}_{0.2}$ device modeled in this work is not necessarily optimized in terms of number of stages and spectral coverage, and it is possible that different configurations (still based on the same materials system) may provide larger values of the extracted power. Even greater improvements can be expected if QW systems with larger conduction-band offsets are employed, so that a larger fraction of the incident radiation spectrum can be absorbed. Two attractive candidates in this respect are $\text{GaN}/\text{Al}(\text{Ga})\text{N}$ and $\text{ZnCdSe}/(\text{Zn})(\text{Cd})\text{MgSe}$ QWs, where the usable barrier height can be as large as 1.75 and 1.2 eV, respectively. While neither materials system has yet reached the same level of maturity for ISB device development as As-based QWs, significant advances have been reported recently, including the demonstration of QCP detection with GaN at the record short wavelength of $1.7 \mu\text{m}$ [14] and the observation of mid-infrared ISB electroluminescence from ZnCdSe [23]. One can therefore expect that further advances in these materials may eventually enable the development of high-performance highly-tunable QCPs, as required for the TPV application considered in this work.

Alternatively, the absorption bandwidth of the InGaAs device under study may be complemented by a p - n junction photovoltaic detector operating at shorter wavelengths. This p - n junction may be grown directly over the n -type multiple-stage QCP structure, which should then be oriented so as to produce a photocurrent flowing towards the top contact. A particularly convenient material choice for the additional n and p layers is $\text{In}_{0.53}\text{Ga}_{0.47}\text{As}$, which is lattice matched to InP and to strain-compensated $\text{In}_{0.7}\text{Ga}_{0.3}\text{As}/\text{AlAs}_{0.8}\text{Sb}_{0.2}$ QWs, and whose bandgap energy of 0.74 eV is above the high-energy end of the combined absorption spectrum of Fig. 2. In fact, such a p - n junction could be employed by itself for TPV energy conversion with reasonable performance [2], which can then be substantially improved by combining it with the ISB device described in this work. Alternatively, an InGaAs alloy of smaller bandgap energy could be employed to further improve the spectral coverage of the incident radiation, possibly in conjunction with suitable buffer layers to accommodate the resulting lattice mismatch.

5. Conclusions

In summary, we have studied the design and limiting performance of QCPs for TPV energy conversion. In general, QCPs provide strong photovoltaic response over a narrow spectral range at geometrically tunable wavelengths. Thus, several QCP stages based on the same QW materials system and designed for absorption over adjacent spectral regions can be grown on top of one another, to produce a high efficiency multiple-junction photovoltaic device. Furthermore, the use of bound-to-continuum ISB transitions allows controlling the absorption bandwidths of the individual stages so as to closely match their output currents, as needed in order to maximize the device output power. The specific materials platform considered in this study is that of strain-compensated $\text{In}_{0.7}\text{Ga}_{0.3}\text{As}/\text{AlAs}_{0.8}\text{Sb}_{0.2}$ QWs, which feature a relatively large conduction-band offset and a well established ISB device technology. An exemplary implementation of a multiple-junction QCP comprising four different stage architectures was designed based on these QWs. The device electrical characteristics were then calculated under the assumptions of unit quantum efficiency throughout the combined absorption bandwidth and of thermal equilibrium within each cascade of highly connected electronic states. Correspondingly, a maximum output power density of 1.4 W/cm^2 in the presence of thermal radiation from a blackbody at 1300 K was computed. This limiting value compares favorably with the present state-of-the-art in TPV energy extraction from a similar thermal source (about 0.8 W/cm^2 as reported in Ref. 5). We conclude that QCP structures, either by themselves or in

combination with interband p - n junction devices, may provide a promising new approach to improve energy extraction efficiency from thermal sources.

Acknowledgements

Partial support for R. P. has been provided by NSF through Grant No. ECCS-0824116.